www.springer.com/41230
https://doi.org/10.1007/s41230-022-2085-z

Microstructure and mechanical properties of as-cast $(CuNi)_{100-x}Co_x$ medium-entropy alloys

Zhi-yong Yang[1, 3], Wei-ping Chen[1, 3], Liang-yan Hao[2], Chen-liang Chu[1, 3], Da-hai Zeng[1, 3], Wei Xiong[2], and *Zhi-qiang Fu[1, 3]

1. Guangdong Key Laboratory for Advanced Metallic Materials Processing, South China University of Technology, Guangzhou 510640, China

2. Physical Metallurgy and Materials Design Laboratory, Department of Mechanical Engineering and Materials Science, University of Pittsburgh, Pittsburgh, PA, 15261, USA

3. National Engineering Research Center of Near-net-shape Forming for Metallic Materials, South China University of Technology, Guangzhou 510640, China

Abstract: Microstructure and mechanical properties of non-equiatomic $(CuNi)_{100-x}Co_x$ (x=15, 20, 25 and 30, at.%) medium-entropy alloys (MEAs) prepared by vacuum arc-melting were investigated. Results show that all the as-cast MEAs exhibit dual face-centered cubic (fcc) solid-solution phases with identical lattice constant, showing typical dendrite structure consisting of (Ni, Co)-rich phase in dendrites and Cu-rich phase in inter-dendrites. The positive enthalpy of mixing among Cu and Ni-Co elements is responsible for the segregation of Cu. With the increase of Co content, the volume fraction of (Ni, Co)-rich phase increases while the Cu-rich phase decreases, resulting in an increment of yield strength and a decrement of elongation for the $(CuNi)_{100-x}Co_x$ MEAs. Nano-indentation test results show a great difference of microhardness between the two fcc phases of the MEAs. The measured microhardness value of the (Ni, Co)-rich phase is almost twofold as compared to that of the Cu-rich phase in all the $(CuNi)_{100-x}Co_x$ MEAs. During the deformation of the MEAs, the Cu-rich phase bears the main plastic strain, whereas the (Ni, Co)-rich phase provides more pronounced strengthening.

Keywords: medium-entropy alloys; microstructure; mechanical properties; nano-indentation

CLC numbers: TG146.1$^+$1; Document code: A; Article ID: 1672-6421(2022)06-511-08

***Zhi-qiang Fu**

Born in 1986, Ph. D, Professor. His research interests mainly focus on alloy design, manufacturing and processing of critical metallic materials used in extreme environments.

E-mail: zhiqiangfu2019@scut.edu.cn

Received: 2022-06-13
Accepted: 2022-09-07

1 Introduction

The discovery of novel alloys is an eternal pursuit in the development of human civilization. Most traditional approaches of developing new alloys are mainly based on one or two principal elements combined with adding modest amounts of other alloying elements, for instance, iron-based, copper-based, and aluminum-based alloys [1]. After thousands of years of exploitation, the alloy design has hit a bottleneck, and it is difficult to explore high-performance alloys through the conventional alloy design concept. Since 2004, a novel strategy of alloy design based on the concept of high-entropy alloys (HEAs), which contain at least five primary metallic elements with each having an atomic proportion ranging from 5at.% to 35at.%, has provided new hope to the materials community [1, 2]. According to the concept of configurational entropy (ΔS_{mix}), alloys can be classified into three categories: HEAs ($\Delta S_{mix} \geq 1.5R$), medium-entropy alloys (MEAs, $1.0R \leq \Delta S_{mix} < 1.5R$), and low-entropy alloys ($\Delta S_{mix} < 1.0R$) [3].

The reason why HEAs/MEAs have attracted considerable attention can be explained by the following two aspects. First, the multi-principal HEAs/MEAs have extensively expanded the alloy design space, offering an endless chance of exploring novel alloys [4]. Second, due to the presence of multi-principal elements, HEAs/MEAs may achieve multiple appealing properties which cannot be attained in conventional alloys [5]. It has been reported that single-phase fcc HEAs/MEAs usually exhibit good ductility, excellent corrosion

resistance and outstanding fracture toughness at cryogenic temperatures [6–8]. Furthermore, their extraordinary ductility and strain-hardening capacity enable them to act as an ideal base alloy for further strengthening [9–13]. Hence, many fcc HEAs/MEAs, such as CrCoNi, VCoNi and FeCrCoNi alloys, have been extensively explored and investigated [9–13].

It has been found that HEAs/MEAs containing high concentration of Cu element could achieve excellent resistance to microbiologically influenced corrosion, due to that the Cu ions released from these alloys could prevent the growth and biofilm formation of biocorrosive marine bacterial species [14–18]. Cu-bearing HEAs/MEAs exhibit significant application potential in a marine environment requiring structure-function integrated materials with excellent mechanical and antimicrobial properties [19]. Nevertheless, rarely few Cu-rich fcc HEAs/MEAs have been explored up to date. As it is known, both Cu-Ni and Ni-Co have infinite solubility, suggesting that Cu-Ni-Co may form fcc solid-solution phases. Consequently, Cu element is used to replace Cr and V elements in the CrCoNi or VCoNi MEAs, aiming at exploring Cu-bearing Cu-Ni-Co MEAs which may display simple solid-solution phases with appealing resistance to microbiologically influenced corrosion. In addition, considering the costly Co element, its content is intentionally lowered down in these MEAs.

In this study, a serious of $(CuNi)_{100-x}Co_x$ MEAs (x=15, 20, 25 and 30, at.%) were designed, and prepared by arc melting, and their phase constitution, microstructure and mechanical behaviors were investigated.

2 Material and methods

2.1 Alloy preparation

The as-cast $(CuNi)_{100-x}Co_x$ (x=15, 20, 25 and 30, at.%) ingots were prepared by vacuum arc-melting using the high-purity elemental particles (purity ≥ 99.95wt.%) as the starting materials, under high-purity argon atmosphere. To ensure chemical homogeneity, ingots with a weight of 90 g were flipped and remelted at least five times. Finally, samples with a dimension of 60 mm (length)×25 mm (width)×12 mm (thickness) were obtained.

2.2 Microstructure and phase constitution

The crystal structure and microstructure of the as-cast alloys were studied using the X-ray diffractometer (XRD), a scanning electron microscope (SEM) and a transmission electron microscope (TEM). Specimens with the geometry of Φ10 mm×1 mm for XRD analysis were firstly ground by SiC papers up to 2000-grit, and then characterized by Panalytical X'Pert using Cu Kα radiation at a scanning angle of 20°–100° and a speed of 2°·min^{-1}. Microstructure observation was performed on a Quanta 650 FEG SEM equipped with backscattered electron (BSE) and energy dispersive spectrometry (EDS) detectors after the specimens were applied to the standard metallographic polishing. Microstructure and phase constitutions of the $(CuNi)_{85}Co_{15}$ and $(CuNi)_{70}Co_{30}$ MEAs were further investigated using a TECNAI G2 S-TWIN F20 (200 kV) TEM equipped with selected area electron diffraction (SAED) and energy dispersive spectroscopy (EDS) detectors.

2.3 Mechanical properties testing

Tensile tests were carried out on a universal testing machine (Zwick/Roell Z020, Germany) at a strain rate of 1×10^{-3} s^{-1} under ambient temperature. For the tests, flattened dog bone specimens with the geometry of 10 mm (gauge length)×2.5 mm (width) ×1 mm (thickness) were cut from ingots by electric discharge machining (EDM). All faces of their gauge sections were ground by 600-grit SiC paper. A digital hardness tester (HVS-1000) was used to determine the Vickers hardness of the specimens with a 300 g load and a holding time of 15 s. The microhardness of the Cu-rich and (Ni, Co)-rich phases of the four studied MEAs was measured using a nano hardness tester (Keysight G200 Nano Indenter). A maximum loading of 30 mN and a holding time of 15 s were used for the testing.

2.4 Thermodynamic calculations

Phase stability of $(CuNi)_{100-x}Co_x$ MEAs was predicted using the CALPHAD (CALculation of PHAse Diagrams) method. Equilibrium step diagrams were calculated using the Thermo-Calc Version 2021b [20] and TCHEA5 high-entropy alloy database.

3 Results and discussion

3.1 XRD results

Figure 1(a) shows the XRD diffraction patterns of the as-cast $(CuNi)_{100-x}Co_x$ MEAs, and the high-magnification image of (200) plane is shown in Fig. 1(b). It can be seen that all the as-cast MEAs exhibit a single set of fcc diffraction peaks. With the increase of Co content, the diffraction peaks of the studied MEAs shift to right slightly, suggesting that the lattice constants of the MEAs decrease gradually. However, as it is known, the diffraction peaks between the phases may overlap and become indistinguishable when the phases present in the alloy have identical crystal structure and extremely close lattice constants. Thus, further characterization is required to confirm the phase constitutions of the as-cast $(CuNi)_{100-x}Co_x$ MEAs.

3.2 SEM and TEM analyses

The BSE images of the as-cast $(CuNi)_{100-x}Co_x$ MEAs are shown in Fig. 2. It can be seen that the microstructures of the as-cast MEAs consist of two distinctive regions with light and dark contrast, which belongs to the typical dendritic structure. Combined with the XRD results, it can be concluded that the MEAs have dual-phase fcc structures and the lattice constants of the two phases are very similar. The chemical compositions of the dendrite (DR) and inter-dendrite (IR) regions of as-cast $(CuNi)_{100-x}Co_x$ MEAs measured by EDS/BSE are listed in Table 1. It can be seen that Ni and Co elements are significantly rich in the dark dendritic regions (fcc1 phase), while Cu element is mainly segregated in the relatively brighter inter-dendritic regions (fcc2 phase). It should be noted that with the increase of Co content, the volume fraction of

(Ni, Co)-rich phase increases, while that of Cu-rich phase decreases. Moreover, the (Ni, Co)-rich dendrites become coarser and tend to merge together, resulting that the Cu-rich phases become disconnected with the increasing of Co content. The EDS maps of the as-cast $Cu_{35}Ni_{35}Co_{30}$ MEA also clearly indicate that the dark dendritic regions are enriched in Ni and Co elements, while the bright inter-dendritic regions are rich in Cu elements, as shown in Fig. 3.

Figure 4 shows TEM images and SAED patterns corresponding to the phases in the as-cast $(CuNi)_{85}Co_{15}$ and $(CuNi)_{70}Co_{30}$ MEAs. The chemical compositions of (Ni, Co)-rich grains and Cu-rich grains measured by EDS/TEM are displayed on TEM images. The corresponding SAED patterns demonstrate that both (Ni, Co)-rich and Cu-rich grains exhibit the typical fcc crystal structure, which is in agreement with the XRD analysis. Consequently, based on the XRD, SEM and TEM analyses, the (Ni, Co)-rich and Cu-rich phases in the MEAs can be identified as fcc1 and fcc2 phases, respectively.

To understand the formation mechanism of the two phases, the mixing enthalpy of atomic pairs and an atom motion model were proposed [21, 22]. Firstly, from a perspective of mixing enthalpy, the mixing enthalpies for Co-Ni, Cu-Co, and Cu-Ni, are 0, 6, and 4 $kJ·mol^{-1}$ [5], respectively. Clearly, Cu-containing binary atom-pairs own the largest enthalpies of mixing. Positive values of mixing enthalpies indicate the immiscibility between Cu and other elements. Hence, Cu element tends to segregate in the inter-dendrite regions and thus forms the fcc2 phase during solidification. Secondly, an atomic motion model can be utilized to describe the phase formation of the MEAs. During the solidification process, Co and Ni elements with relative higher melting points (Co: 1,768 K; Ni: 1,726 K [5]) firstly solidified from the liquid to form the primary (Co, Ni)-rich phase. As the temperature decreases, the Cu element with relatively low melting point (Cu: 1,356 K [5]) solidified via peritectic reaction

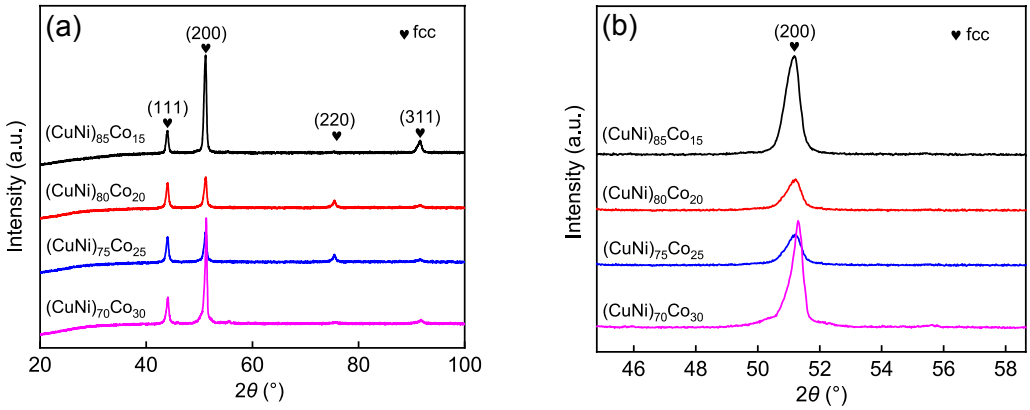

Fig. 1: XRD patterns of as-cast $(CuNi)_{100-x}Co_x$ MEAs (a), and high-magnification of (200) plane (b)

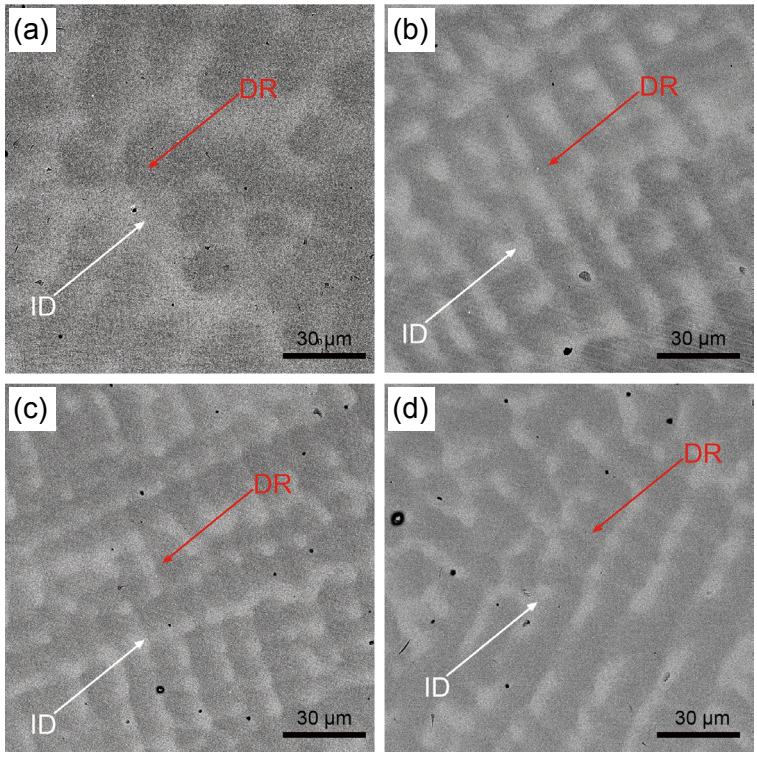

Fig. 2: BSE images of as-cast $(CuNi)_{100-x}Co_x$ MEAs: (a) $(CuNi)_{85}Co_{15}$; (b) $(CuNi)_{80}Co_{20}$; (c) $(CuNi)_{75}Co_{25}$; (d) $(CuNi)_{70}Co_{30}$

Table 1: Chemical compositions of different regions in as-cast $(CuNi)_{100-x}Co_x$ MEAs measured by EDS/TEM

Alloys	Regions	Crystal structure	Chemical composition (at.%)		
			Cu	Ni	Co
$(CuNi)_{85}Co_{15}$	Nominal		42.50	42.50	15.00
	Dendrite	fcc1	35.68	46.12	18.20
	Inter-dendrite	fcc2	62.86	29.06	8.08
$(CuNi)_{80}Co_{20}$	Nominal		40.00	40.00	20.00
	Dendrite	fcc1	31.95	43.47	24.59
	Inter-dendrite	fcc2	60.35	28.27	11.38
$(CuNi)_{75}Co_{25}$	Nominal		37.50	37.50	25.00
	Dendrite	fcc1	29.52	40.54	29.94
	Inter-dendrite	fcc2	61.84	25.13	13.04
$(CuNi)_{70}Co_{30}$	Nominal		35.00	35.00	30.00
	Dendrite	fcc1	24.34	37.97	37.70
	Inter-dendrite	fcc2	72.49	17.83	9.68

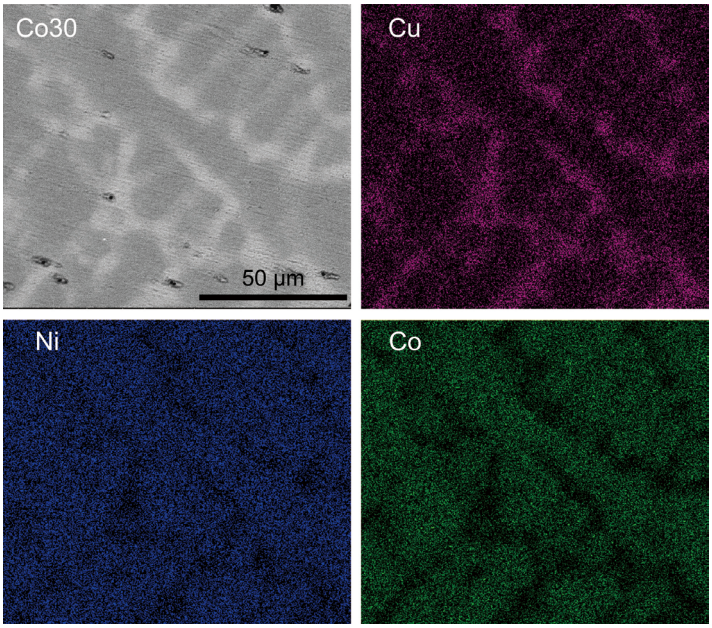

Fig. 3: BSE image and EDS maps of the as-cast $(CuNi)_{70}Co_{30}$ MEA

with the primary (Co, Ni)-rich phase, i.e., forming Cu-rich inter-dendritic phase. In addition, the Ni-Co and Cu-Ni have completely mutual solubilities, leading to the presence of high content of Cu in the (Co, Ni)-rich fcc1 phase and high contents of Ni-Co in the Cu-rich fcc2 phase.

Many empirical guidelines have been used to evaluate the phase formation ability or stability of multi-component HEAs/MEAs including atomic-size difference (δ), the mixing entropy (ΔH_{mix}), mixing enthalpy (ΔS_{mix}), entropy-enthalpy ratio (Ω), valence electron concentration (VEC), etc. Zhang et al. [23–26] revealed that solid-solution phases rather than intermetallic compounds would form when $\Omega \geq 1.1$ and $\delta \leq 6.6\%$. These empirical parameters were used to evaluate the studied MEAs. The ratio of the entropy to enthalpy of mixing (Ω) is expressed by the following equation [23–26]:

$$\Omega = \frac{T_m \Delta S_{mix}}{|\Delta H_{mix}|} \quad (1)$$

where T_m is the mean melting point of the elements, T_m, ΔS_{mix}, and ΔH_{mix} can be calculated by the following equations:

$$T_m = \sum_{i=1}^{n} c_i T_i \quad (2)$$

$$\Delta S_{mix} = -R \sum_{i=1}^{n} c_i \ln c_i \quad (3)$$

$$\Delta H_{mix} = \sum_{i=1, i \neq j}^{n} 4 \Delta H_{ij}^{mix} c_i c_j \quad (4)$$

where n represents the quantity of component elements, c_i and T_i are the atomic percentage and melting point of the ith element, R and H_{ij}^{mix} are the universal gas constant and the enthalpy of mixing of the ith and jth elements, respectively. The atomic-size difference (δ) is calculated by Eq. (5) [23–26]:

$$\delta = \sqrt{\sum_{i=1}^{n} c_i \left(1 - r_i / \sum_{i=1}^{n} c_i r_i\right)^2} \quad (5)$$

where r_i represents the radius of the ith constituent element. The calculated values of Ω and δ of the $(CuNi)_{100-x}Co_x$ MEAs by Eqs. (1)–(5) are shown in Table 2. Clearly, according to the above-mentioned criteria, the studied MEAs should form solid-solution phases, which is in agreement with our experimental results. Guo et al. [27] suggested that valance electron concentration plays a vital role in predicting the phase stability of the HEAs/MEAs. This criterion

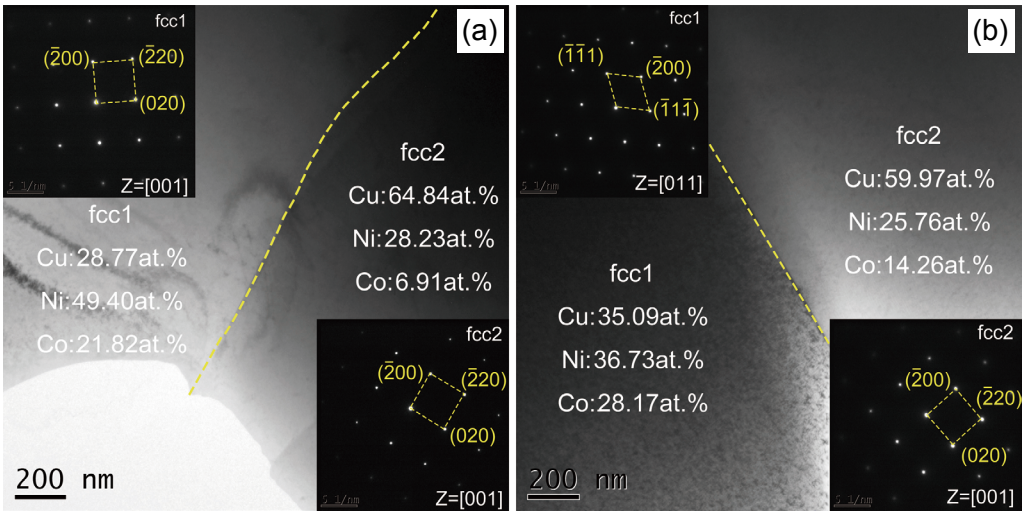

Fig. 4: TEM images of as-cast $(CuNi)_{100-x}Co_x$ MEAs: (a) $(CuNi)_{85}Co_{15}$; (b) $(CuNi)_{70}Co_{30}$. The inset images showing SAED patterns corresponding to fcc1 and fcc2, respectively

reveals that fcc phase is stabilized when VEC≥8, whereas bcc phase becomes more stable when VEC<6.87. The values of VEC for the $(CuNi)_{100-x}Co_x$ MEAs, as shown in Table 2, indicate the studied MEAs can form stabilized fcc solid-solution phases.

It is worth mentioning that the existence of metastable liquid-liquid separation in Cu-Co binary alloy systems has been reported [28–30]. The microstructure of the solidified alloy with liquid-liquid separation was characterized by a sphere of one phase surrounded by a matrix of the other phase [28–30]. When the supercooled melt lowered to a fixed temperature approaching to the liquid miscibility gap (binodal), it could be separated into two liquids, i.e., Cu-rich and Co-rich liquids. The occurrence of liquid-liquid separation is a reflection of the interplay of the energetic and structural rearrangement of the constituent elemental atoms, which can be interpreted by mixing enthalpy [31, 32]. In Cu-Co binary alloy, mixing enthalpies between Cu and Co are positive (Cu-Co: +6 kJ·mol^{-1}), suggesting that Cu element has repulsive interactions with Co element. In the present work, liquid-liquid separation is not observed, which could be explained as follows: firstly, the undercooling of the MEAs fabricated by arc melting during cooling does not reach the critical value of undercooling for liquid-liquid separation. Secondly, Sun et al. [29] found that adding Ni atoms into Cu-Co could suppress the liquid-liquid separation, thereby leading to decreased volume fraction of Co-rich particles in the Cu-rich matrix. In addition, Curiotto et al. [30] found that the temperature for the occurrence of metastable liquid phase separation in Cu-Co would be lowered by 12 K per at.% of Ni addition. Therefore, it can be inferred that the failure of undercooling reaching a critical value and the addition of Ni synergistically lead to the absence of the liquid-liquid separation phenomenon in the present work.

3.3 Thermodynamic prediction of phase constitution of $(CuNi)_{100-x}Co_x$ MEAs

Figures 5 (a–d) are the equilibrium diagrams of the $(CuNi)_{100-x}Co_x$ MEAs showing the equilibrium phase fraction as a function of temperature. The calculated liquidus and solidus temperatures of $(CuNi)_{100-x}Co_x$ MEAs increase as the Co concentration increases. For example, the liquidus temperatures are 1,619 K; 1,634 K; 1,649 K; and 1,663 K for the $(CuNi)_{85}Co_{15}$, $(CuNi)_{80}Co_{20}$, $(CuNi)_{75}Co_{25}$, and $(CuNi)_{70}Co_{30}$ MEAs, respectively, whereas the solidus temperatures are 1,539 K; 1,544 K; 1,551 K; and 1,560 K, respectively. It is owing to the higher melting point of Co than those of Cu and Ni. As shown in Fig. 5, all MEAs exhibit the single fcc phase region below the solidus temperature. When the temperature decreases, the single fcc phase decomposes into two fcc phases, with one rich in Co and Ni while another rich in Cu, which is in line with our experimental results. Meanwhile, it is evident from Fig. 5 that as the content of Co increases, the fraction of (Ni, Co)-rich fcc phase increases, and that of Cu-rich fcc decreases. In summary, the present thermodynamic calculations satisfactorily validate the experimental observations.

Table 2: Calculated values for T_m, ΔS_{mix}, ΔH_{mix}, Ω, δ, and VEC

Alloys	T_m (K)	ΔS_{mix} (kJ·mol^{-1})	ΔH_{mix} (kJ·mol^{-1})	Ω	δ	VEC
$(CuNi)_{85}Co_{15}$	1,575	8.41	4.42	3.00	1.10	10.28
$(CuNi)_{80}Co_{20}$	1,587	8.77	4.48	3.11	1.07	10.20
$(CuNi)_{75}Co_{25}$	1,598	9.00	4.50	3.19	1.04	10.13
$(CuNi)_{70}Co_{30}$	1,609	9.11	4.48	3.27	1.01	10.05

3.4 Mechanical properties

The tensile engineering stress-strain curves of the as-cast $(CuNi)_{100-x}Co_x$ MEAs at room temperature are shown in Fig. 6(a). The yield strength and Vickers hardness of the as-cast $(CuNi)_{100-x}Co_x$ MEAs as a function of Co content are illustrated in Fig. 6(b). Evidently, with the increase of Co content, the yield strength increases linearly, and the Vickers hardness also displays an increasing trend. Table 3 lists the specific values of yield strength (YS), ultimate tensile strength (UTS) and elongation (El) of the as-cast $(CuNi)_{100-x}Co_x$ MEAs. The $(CuNi)_{70}Co_{30}$ MEA with the highest Co content shows the maximum yield strength (384 MPa) and the lowest elongation (1.9%), whereas the $(CuNi)_{85}Co_{15}$ MEA with the lowest Co content exhibits the lowest yield strength (242 MPa) and the highest elongation (15.5%).

As mentioned above, with the increase of Co content in $(CuNi)_{100-x}Co_x$ MEAs, the volume fraction of the (Ni, Co)-rich (fcc1) phase increases while the volume fraction of the Cu-rich (fcc2) phase decreases. Based on the statistical analyses of BSE images using IamgeJ software, as the Co content increases from 15at.% to 20at.%, 25at.%, and 30at.%, the volume fraction of the (Ni, Co)-rich fcc1 phase in the $(CuNi)_{100-x}Co_x$ MEAs is estimated to be 71.9vol.%, 75.6vol.%, 81.0vol.% and 84.9vol.%, respectively, and the volume fraction of the Cu-rich fcc2 phase is estimated to be 28.1vol.%, 24.4vol.%, 19.0vol.% and 15.1vol.%, respectively. Accordingly, the yield strength and Vickers hardness of the

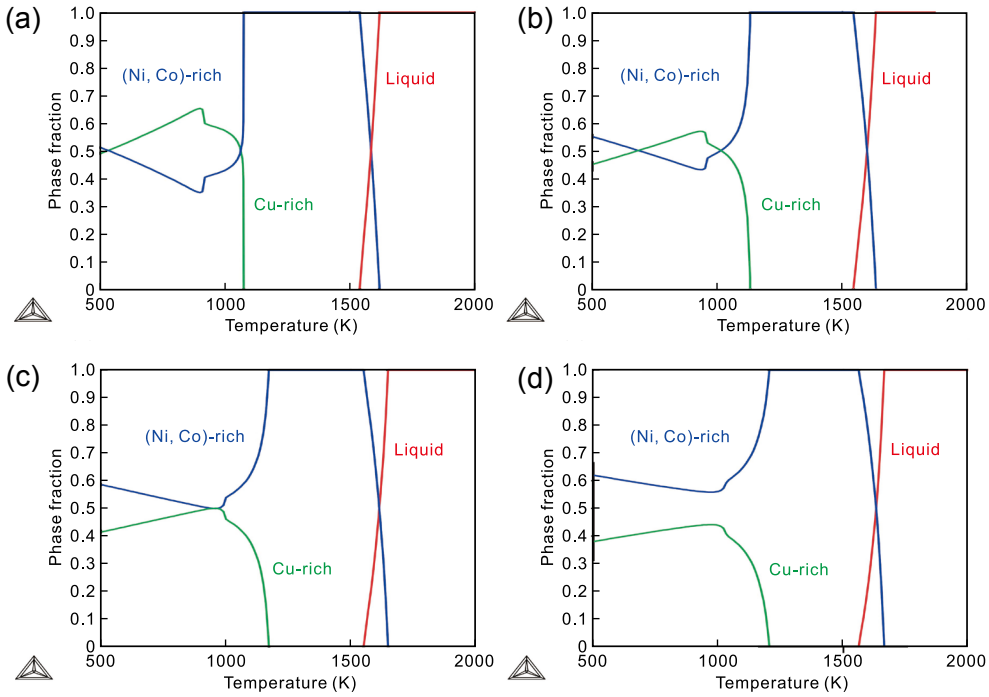

Fig. 5: Simulated equilibrium phase diagrams of $(CuNi)_{100-x}Co_x$ MEAs: (a) $(CuNi)_{85}Co_{15}$; (b) $(CuNi)_{80}Co_{20}$; (c) $(CuNi)_{75}Co_{25}$; (d) $(CuNi)_{70}Co_{30}$

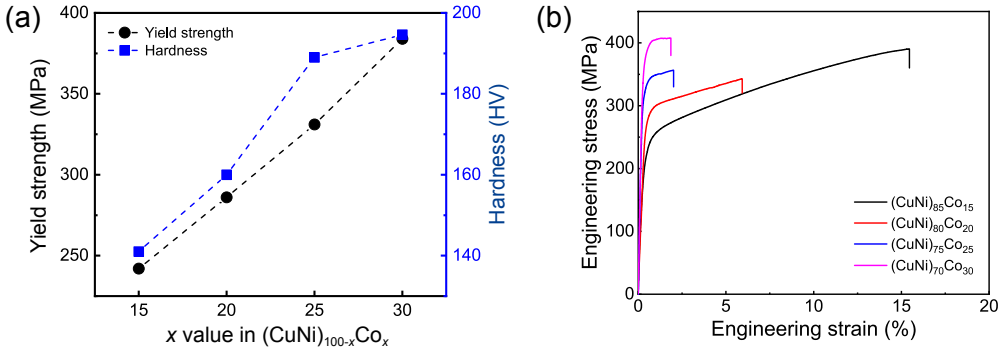

Fig. 6: Engineering tensile stress-strain curves (a), and yield strength and Vickers hardness (b) of as-cast $(CuNi)_{100-x}Co_x$ MEAs as a function of Co content

Table 3: Mechanical properties of as-cast $(CuNi)_{100-x}Co_x$ MEAs

Alloys	YS (MPa)	UTS (MPa)	El (%)	Hardness (HV)
$(CuNi)_{85}Co_{15}$	242	390	15.5	141
$(CuNi)_{80}Co_{20}$	286	342	5.9	160
$(CuNi)_{75}Co_{25}$	331	356	2.0	189
$(CuNi)_{70}Co_{30}$	384	407	1.9	194

MEAs should be dominated by the volume fractions of the fcc1 and fcc2 phases. To further understand the relationship between the mechanical properties of the (Ni, Co)-rich fcc1 and Cu-rich fcc2 phase, nanoindentation tests were performed on the as-cast $(CuNi)_{100-x}Co_x$ MEAs. The typical nano-indentation loading-displacement curves of the (Ni, Co)-rich and Cu-rich phases in the $(CuNi)_{100-x}Co_x$ MEAs at room temperature are shown in Fig. 7. Table 4 lists the indentation hardness values of the (Ni, Co)-rich and Cu-rich phases for each MEA calculated from the curves. With the increase of Co content, the indentation hardnesses of Cu-rich phase in the as-cast $(CuNi)_{100-x}Co_x$ MEAs are 3.567, 3.569, 3.445 and 3.272 GPa, respectively, and the indentation hardness of (Ni, Co)-rich phase are 5.836, 6.056, 5.448 and 6.590 GPa, respectively. Evidently, as the Co content increases, the indentation hardness of the Cu-rich phase in the $(CuNi)_{100-x}Co_x$ MEAs gradually decreases, whereas the indentation hardness of the (Ni, Co)-rich phase gradually increases with the exception of $(CuNi)_{75}Co_{25}$. The hardness value of the (Ni, Co)-rich fcc1 phase is almost twofold as that of the Cu-rich fcc2 phase, demonstrating the large property gap between the two phases. Combined with the elongation values in Table 3, the Cu-rich phase in the $(CuNi)_{100-x}Co_x$ MEAs is soft and tough, in contrast, the (Ni, Co)-rich phase is hard but brittle. Hence, The Cu-rich phase bears the main plastic strain during the deformation process.

In addition, the (Ni, Co)-rich phase provides more strengthening contribution to the as-cast $(CuNi)_{100-x}Co_x$ MEAs. As the Co content increases, the volume fraction of the (Ni, Co)-rich phase in the $(CuNi)_{100-x}Co_x$ MEAs increases, resulting in increased yield strength and reduced ductility. Therefore, the brittleness of the $(CuNi)_{75}Co_{25}$ and $(CuNi)_{70}Co_{30}$ MEAs (Table 3) should be ascribed to the reduction of Cu-rich phase.

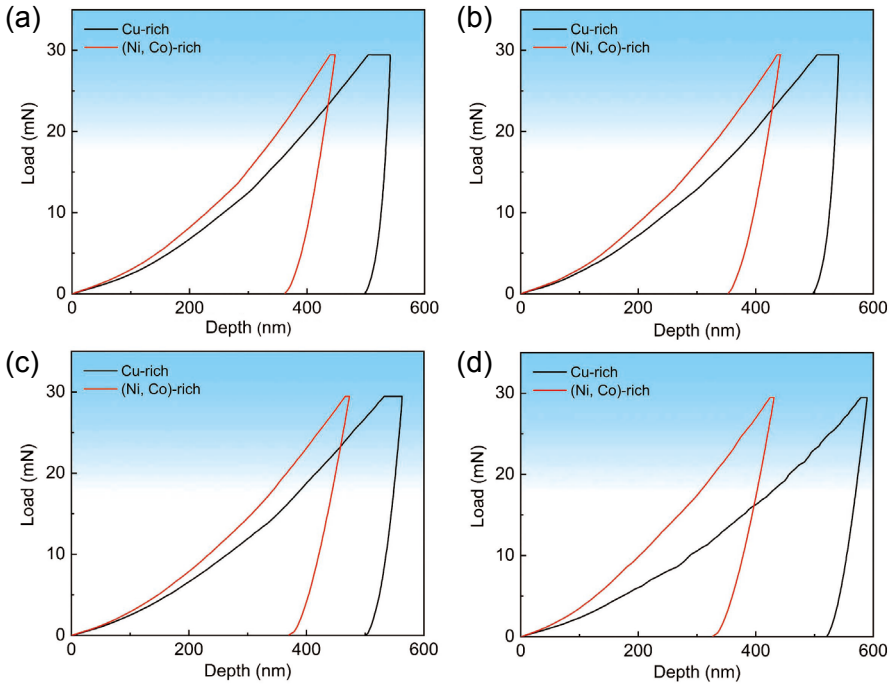

Fig. 7: Fitting relationship between load and pressure depth of as-cast $(CuNi)_{100-x}Co_x$ MEAs: (a) $(CuNi)_{85}Co_{15}$; (b) $(CuNi)_{80}Co_{20}$; (c) $(CuNi)_{75}Co_{25}$; (d) $(CuNi)_{70}Co_{30}$

Table 4: Indentation hardness of as-cast $(CuNi)_{100-x}Co_x$ MEAs

Phase	Indentation hardness (GPa)			
	$(CuNi)_{85}Co_{15}$	$(CuNi)_{80}Co_{20}$	$(CuNi)_{75}Co_{25}$	$(CuNi)_{70}Co_{30}$
Cu-rich	3.567	3.569	3.445	3.272
(Ni, Co)-rich	5.836	6.056	5.448	6.590

4 Conclusions

In the present work, microstructure and mechanical properties of the $(CuNi)_{100-x}Co_x$ (x=15, 20, 25 and 30, at.%) MEAs prepared by vacuum arc-melting were systematically investigated. The main conclusions are summarized as follows:

(1) The as-cast $(CuNi)_{100-x}Co_x$ MEAs exhibit dual fcc phases with typical dendrite structure, consisting of a (Ni, Co)-rich phase (fcc1) in the dendrite region and a Cu-rich phase (fcc2) in the interdendrite region. In addition, the two fcc phases exhibit identical lattice constant. With the increase of Co content, the volume fraction of the (Ni, Co)-rich (fcc1) phase increases, while that of the Cu-rich (fcc2) phase decreases.

(2) The large positive mixing enthalpy of Cu-Co and the lowest melting point among Ni, Co and Cu, are responsible for the segregation of Cu, and the formation of (Ni, Co)-rich dendrites and Cu-rich interdendrites during solidification.

(3) With the increase of Co content, the yield strength of the as-cast $(CuNi)_{100-x}Co_x$ MEAs increases from 242 MPa to 384 MPa, whereas the

total elongation decreases from 15.5% to 1.9%. The (Ni, Co)-rich fcc1 phase and Cu-rich fcc2 phase show a great difference in indentation hardness value, that is, the hardness of (Ni, Co)-rich phase is almost twofold that of the Cu-rich phase. Therefore, as the Co content increases, the increase in volume fraction of the (Ni, Co)-rich phase results in the increased yield strength and reduced ductility.

Acknowledgements

This work was financially supported by the Key-Area Research and Development Program of Guangdong Province (Grant No. 2018B090905002), the National Natural Science Foundation of China (Grant No. 52103360), and the Basic Research Foundation of Guangzhou City (Grant No. 201804020071). Liang-yan Hao and Wei Xiong performed the thermodynamic modeling without funding support.

References

[1] Yeh J W, Chen S K, Lin S J, et al. Nanostructured high-entropy alloys with multiple principal elements: Novel alloy design concepts and outcomes. Advanced Engineering Materials, 2004, 6(5): 299–303.
[2] Ma X N, Hu Y F, Wang K, et al. Microstructure and mechanical properties of a low activation cast WTaHfTiZr refractory high-entropy alloy. China Foundry, 2022. https://doi.org/10.1007/s41230-022-1230-z.
[3] Moon J, Park J M, Bae J W, et al. A new strategy for designing immiscible medium-entropy alloys with excellent tensile properties. Acta Materialia, 2020, 193: 71–82.
[4] Li W, Xie D, Li D, et al. Mechanical behavior of high-entropy alloys. Progress in Materials Science, 2021, 118: 100777.
[5] Miracle D B, Senkov O N. A critical review of high entropy alloys and related concepts. Acta Materialia, 2017, 122: 448–511.
[6] Gludovatz B, Hohenwarter A, Catoor D, et al. A fracture-resistant high-entropy alloy for cryogenic applications. Science, 2014, 345(6201): 1153–1158.
[7] Yao M J, Pradeep K G, Tasan C C, et al. A novel, single phase, non-equiatomic FeMnNiCoCr high-entropy alloy with exceptional phase stability and tensile ductility. Scripta Materialia, 2014, 72: 5–8.
[8] Wu Z, Bei H, Pharr G M, et al. Temperature dependence of the mechanical properties of equiatomic solid solution alloys with face-centered cubic crystal structures. Acta Materialia, 2014, 81: 428–441.
[9] Zhao Y L, Yang T, Tong Y, et al. Heterogeneous precipitation behavior and stacking-fault-mediated deformation in a CoCrNi-based medium-entropy alloy. Acta Materialia, 2017, 138: 72–82.
[10] Tian J, Tang K, Wu Y K, et al. Effects of Al alloying on microstructure and mechanical properties of VCoNi medium entropy alloy. Materials Science and Engineering: A, 2021, 811: 141054.
[11] Moravcik I, Hadraba H, Li L, et al. Yield strength increase of a CoCrNi medium entropy alloy by interstitial nitrogen doping at maintained ductility. Scripta Materialia, 2020, 178: 391–397.
[12] Lin Q, Liu J, An X, et al. Cryogenic-deformation-induced phase transformation in an FeCoCrNi high-entropy alloy. Materials Research Letters, 2018, 6(4): 236–243.
[13] Gwalani B, Gorsse S, Choudhuri D, et al. Tensile yield strength of a single bulk $Al_{0.3}$CoCrFeNi high entropy alloy can be tuned from 160 MPa to 1800 MPa. Scripta Materialia, 2019, 162: 18–23.
[14] Gao J B, Jin Y T, Fan Y Q, et al. Fabricating antibacterial CoCrCuFeNi high-entropy alloy via selective laser melting and in-situ alloying. Journal of Materials Science & Technology, 2022, 102(7): 159–165.
[15] Ren G Y, Huang L L, Hu K L, et al. Enhanced antibacterial behavior of a novel Cu-bearing high-entropy alloy. Journal of Materials Science & Technology, 2022, 117: 158–166.
[16] Zhou E Z, Ren G Y, Sun Y L, et al. Antibacterial activities of a novel Cu-bearing high-entropy alloy against multi-drug-resistant Acinetobacter baumannii and Staphylococcus aureus. Rare Metals, 2022, 41(2): 570–579.
[17] Chen C, Chen J L, Yuan S H, et al. Microstructure, mechanical properties, corrosion resistance and anti-bacterial behavior of novel Co-free high entropy alloys. Journal of Alloys and Compounds, 2022, 902: 163714.
[18] Zhou E Z, Qiao D X, Yang Y, et al. A novel Cu-bearing high-entropy alloy with significant antibacterial behavior against corrosive marine biofilms. Journal of Materials Science & Technology, 2020, 46: 201–210.
[19] Yu Y, Xu N N, Zhu S Y, et al. A novel Cu-doped high entropy alloy with excellent comprehensive performances for marine application. Journal of Materials Science & Technology, 2021, 69: 48–59.
[20] Andersson J O, Helander T, Höglund L, et al. Thermo-Calc & DICTRA, computational tools for materials science. Calphad, 2002, 26: 273–312.
[21] Qin G, Chen R, Liaw P K, et al. A novel face-centered-cubic high-entropy alloy strengthened by nanoscale precipitates. Scripta Materialia, 2019, 172: 51–55.
[22] Qin G, Chen R, Mao H, et al. Experimental and theoretical investigations on the phase stability and mechanical properties of $Cr_7Mn_{25}Co_9Ni_{23}Cu_{36}$ high-entropy alloy. Acta Materialia, 2021, 208: 116763.
[23] Feng R, Gao M C, Lee C, et al. Design of light-weight high-entropy alloys. Entropy, 2016, 18(9): 333.
[24] Zhang Y, Lu Z P, Ma S G, et al. Guidelines in predicting phase formation of high-entropy alloys. MRS Communications, 2014, 4(2): 57–62.
[25] Zhang Y, Zhou Y J, Lin J P, et al. Solid-solution phase formation rules for multi-component alloys. Advanced Engineering Materials, 2008, 10(6): 534–538.
[26] Yang X, Zhang Y. Prediction of high-entropy stabilized solid-solution in multi-component alloys. Materials Chemistry and Physics, 2012, 132(2–3): 233–238.
[27] Guo S, Ng C, Lu J, et al. Effect of valence electron concentration on stability of fcc or bcc phase in high entropy alloys. Journal of Applied Physics, 2011, 109(10): 103505.
[28] Nakagawa Y. Liquid immiscibility in copper-iron and copper-cobalt systems in the supercooled state. Acta Metallurgica,1958, 6(11): 704–711.
[29] Sun Z B, Song X P, Hu Z D, et al. Effects of Ni addition on liquid phase separation of Cu-Co alloys. Journal of Alloys and Compounds, 2001, 319(1–2): 276–279.
[30] Curiotto S, Battezzati L, Johnson E, et al. Thermodynamics and mechanism of demixing in undercooled Cu-Co-Ni alloys. Acta Materialia, 2007, 55(19): 6642–6650.
[31] Singh R N, Sommer F. Segregation and immiscibility in liquid binary alloys. Reports on Progress in Physics, 1997, 60(1): 57.
[32] Guo T, Li J S, Wang J, et al. Liquid-phase separation in undercooled CoCrCuFeNi high entropy alloy. Intermetallics, 2017, 86: 110–115.